Supporting Information

Hong et al. 10.1073/pnas.1115803109

SI Text

Simulations. The directed self-assembly of cylindrical microdomains observed in our studies was also confirmed by density functional theory simulations. We numerically integrated the Cahn-Hilliard-Cook diffusion equation with a Landau-Ginzburg free energy expansion (1), where the PS (A) and PEO (B) segmental interactions, the conformations of the block copolymers, and the influence of the solvents were implicitly taken into account in the expansion coefficients (2). The volume fraction of the minority A-block was assumed to be 0.3 and the product of the A-B segmental interaction parameter χ and the chain length N is set to be $\chi N = 20$, ensuring the formation of cylindrical microdomains in the bulk. Based on previous studies (3,4), the geometry of the patterned substrate was modeled to have a pitch of λ and an amplitude of h in a discredited space with a unit spacing $a \cong L_1/8$. The faceted substrate is assumed to preferentially interact with the minority A-block, and the solvent vapor at the upper surface of the film is taken to be energetically neutral to both blocks. Fig. 2*C*–*F* shows the simulation results of the cylindrical microdomains on a faceted surface having an amplitude $h = 0.38L_1$ and pitch $\lambda = 1.7L_1 (= 1.47L_2)$ with a film thicknesses of $\Delta = 1.0L_1$ (Fig. 2*C* and 2*D*) and $\Delta = 1.1L_1$ (Fig. 2*E* and 2*F*). The simulated morphology in Fig. 2*E* shows hemi-cylinders oriented normal to the facet direction form at the surface that are guided by short half cylinders in the valleys of the facets, as seen in Fig. 2*F*. The perpendicular orientation of cylinders with respect to the ridge direction can avoid strong deformation of the unit cell that is intrinsic to the packing of the cylindrical microdomains since the cylinder packing along the ridge direction is unconfined by the topography of the facets. An orientation of the cylindrical microdomains parallel to the ridge direction would also introduce a frustration due to the commensurability between the characteristic spacing of the cylindrical microdomains and the pitch of the facets and, to the nonuniform thickness of the film. It should be noted that disconnected cylindrical microdomains form with thinner films (Fig. 2*C*), as observed experimentally. The discontinuity of these cylindrical microdomains arises from the formation of brush-like domains on the crests of the facets (Fig. 2*D*). As the film becomes thinner, the ridge perturbs the unit cell of cylinders at the film surface causing a disruption of the cylinders. It is also important to note that the morphologies observed in the simulations and experimentally, optimize favorable and minimize nonfavorable interactions between the blocks of the BCP and the substrate.

Slope Error. In Fig. S5, the curves (*B*) and (*C*) have similar root-mean-square roughness. However, if the tangent at each point is calculated, and the root-means-square deviation away from the (in this case) horizontal is determined, then a deviation of the slope away from zero will result. Therefore, the slope error of (*B*) is much larger than that of (*C*), indicating that (*B*) has a higher frequency waviness. The same holds true for curves (*D*) and (*E*) where (*E*) has a higher frequency waviness. A perfectly straight line has a slope error of 0°. A similar analysis can be applied to the cylindrical or lamellar microdomains to assess the waviness (or straightness) of the cylinders.

To calculate the slope error, the corresponding SFM image is imported and the line patterns are traced. The traced line patterns are saved by a list of x-y coordinates along the line selection, which yields 1-dimensional representation of one-line patterns. The same process at different locations is iterated to get more 1-dimensional line patterns for better statistics. The final slope error is an average of the slope error of four different traces.

Orientation Parameter (GI-SAXS and Transmission SAXS) in Case of 2D Objects Within a Thin Film. The orientation parameter, f, is given by $2\langle\cos^2\Psi\rangle - 1$, where Ψ is the rotation angle and $\langle\cos^2\Psi\rangle$ is $\frac{\int I(\Psi)\cos^2\Psi d\Psi}{\int I(\Psi) d\Psi} = \frac{\sum I(\Psi)\cos^2\Psi}{\sum I(\Psi)}$.

The Effect of Roughness of the Faceted Substrate on GI-SAXS Measurements. Whether the surface is smooth or rough the surface is defined as a plane characteristic of the average height of the surface. The facets have incidence angles greater than and less than the critical angle of the radiation on the surface. However, the amplitude of the facets is several nanometers in magnitude and the pitch of the facets is tens of nanometers in size. The pitch is far less than the coherence length of the X-rays on the surface (microns) and, as such, an average value can be used to describe the surface. This does not mean that the facets will not reflect the X-rays at different angles. In fact, when the X-rays are incident on the surface parallel to the facets, reflections are seen characteristic of the facet angles (see Fig. S7). However, like with any rough surface, an average height can be defined and off-specular scattering will occur due to the reflection of the X-rays. This, though, will not affect the interpretation of the scattering arising from the cylindrical microdomains.

1. Gunton JD, Miguel MS, Sahni PS *Phase Transitionsand Critical Phenomena* Vol. 8 (1983), eds Domb C, Lebowitz JN (Academic Press, New York and London).
2. Fredrickson GH, Leibler L (1989) Theory of block copolymer solutions: Nonselective good solvents. *Macromolecules* 22:1238–1250.
3. Huth M, Ritley KA, Oster J, Dosch H, Adrian H (2002) Highly ordered Fe and Nbstripe arrays on facetted α-Al2O3 (1010). *Adv Funct Mater* 12:333–338.
4. Gabai R, Ismach A, Joselevich E (2007) Nanofacet lithography: A new bottom-up approach to nanopatterning and nanofabrication by soft replication of spontaneously faceted crystal surfaces. *Adv Mater* 19:1325–1330.

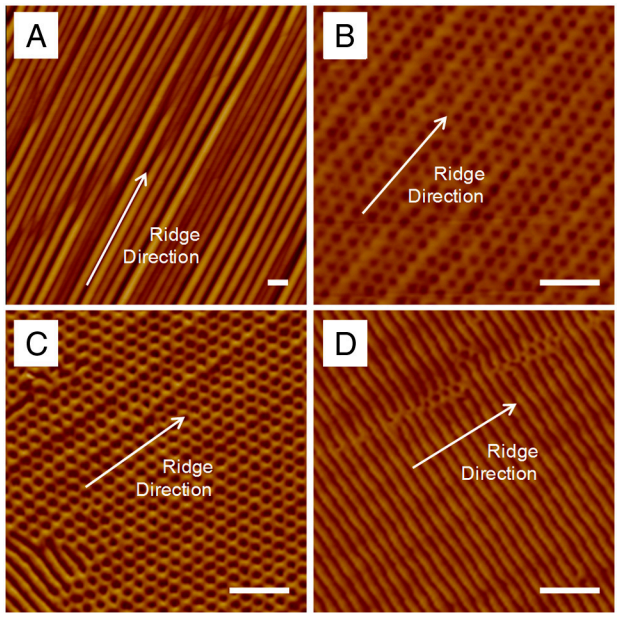

Fig. S1. (*A*) SFM height image of the faceted sapphire substrate. SFM phase images of PS-*b*-PEO ($M_n = 26.5$ kg/mol) thin films on the faceted sapphire substrate. (*B*) The film thickness is 38.0 nm and the solvent annealing time is 0.5 h; (*C*) the film thickness is 38.0 nm and the solvent annealing time is 1.0 h; (*D*) the film thickness is 47.6 nm and the solvent annealing time is 1.5 h. The scale bars are 200 nm.

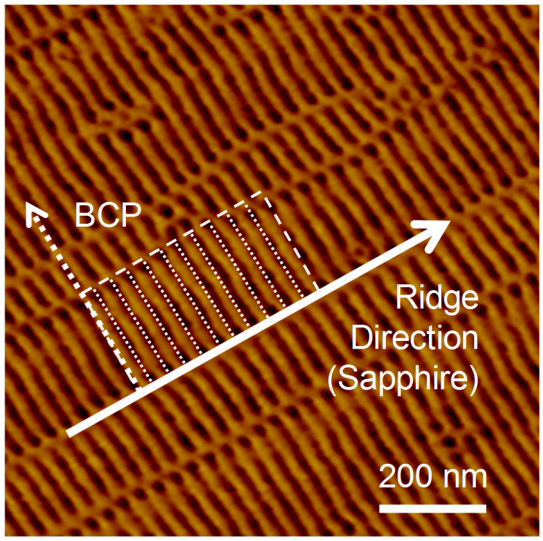

Fig. S2. A diagram overlaid on the data in Fig. 2*A* showing the ridge direction and the direction of the cylindrical microdomains.

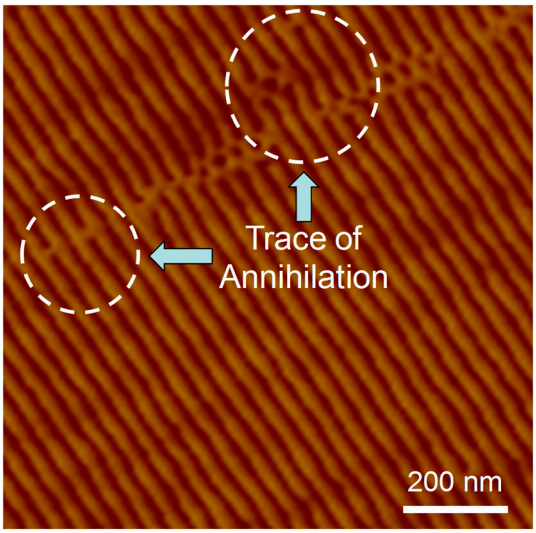

Fig. S3. Highlights of the mechanism of annihilation of defects between the microdomains for the data in Fig. S1*D*.

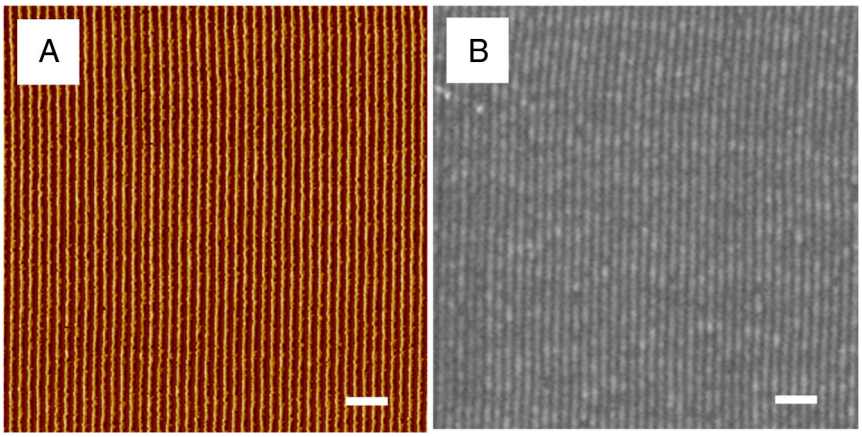

Fig. S4. (*A*) SFM phase image of PS-*b*-P2VP (M_n = 58.0 kg/mol) thin films on the faceted sapphire substrate. (*B*) SEM image of transferred crosslinked siloxane replica released from BCP template. The scale bars are 200 nm.

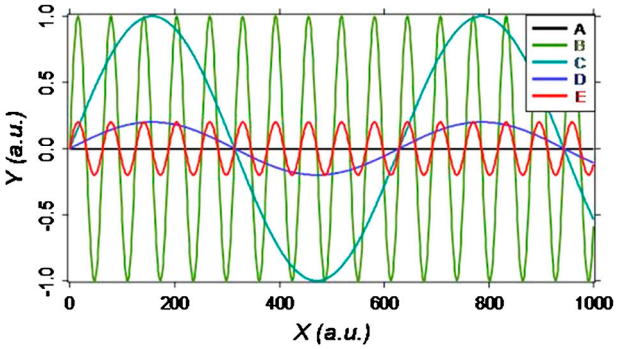

Fig. S5. The graphical illustrations of examples for the slope errors. The slope errors of (*A*), (*B*), (*C*), (*D*), and (*E*) are corresponding to 0°, 4.0°, 0.4°, 0.1°, and 0.8°, respectively.

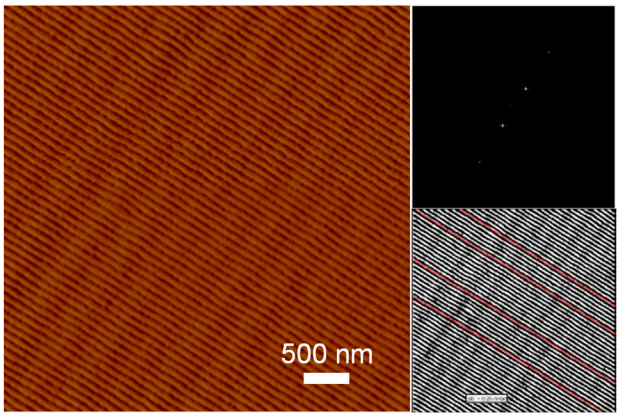

Fig. S6. Cylindrical microdomains (PS-*b*-PEO); $M_n = 26.5$ kg/mol) oriented normal to the ridge direction.

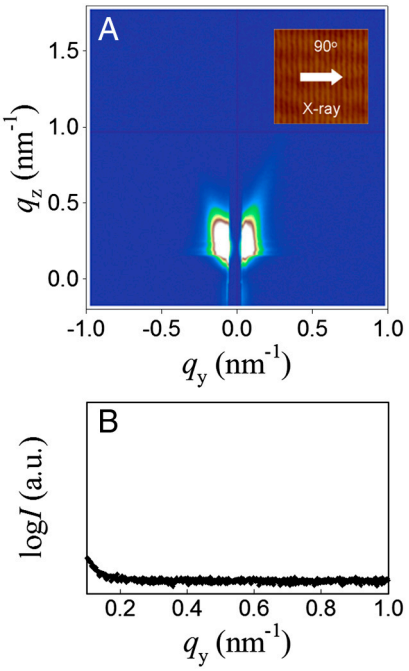

Fig. S7. (*A*) GI-SAXS pattern of PS-*b*-PEO thin film on a faceted sapphire substrate, where the X-ray beam is in the direction of the ridges of the facets. (*B*) The line profile of scattering as a function of the scattering vector shown in Fig. S6*A*. q_y is the in-plane scattering vector.

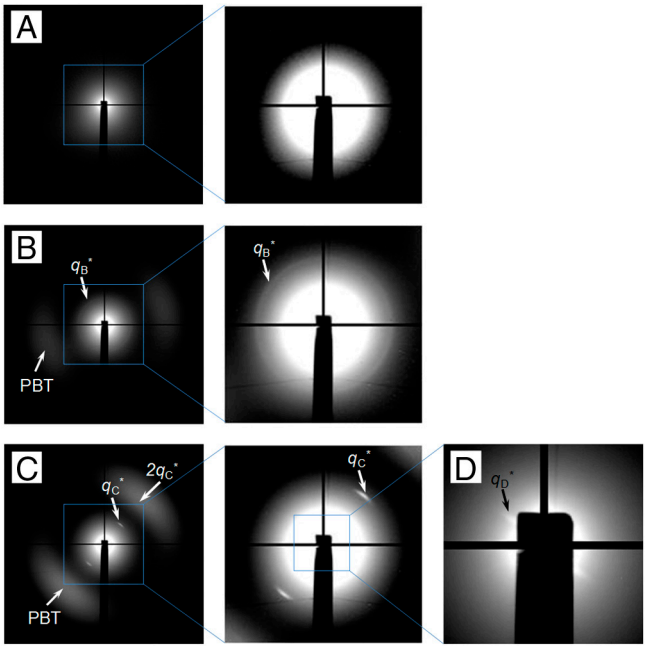

Fig. S8. 2D Transmission SAXS results of PS-*b*-PEO thin films on (*B*) a flat PBT film ($q_B^* = 0.186$ nm^{-1}) and (*C*) a faceted PBT film ($q_C^* = 0.185$ nm^{-1}). (*A*) The background without BCP film and PBT film and (*D*) the magnified area near the beamstop in Fig. S8*C*.

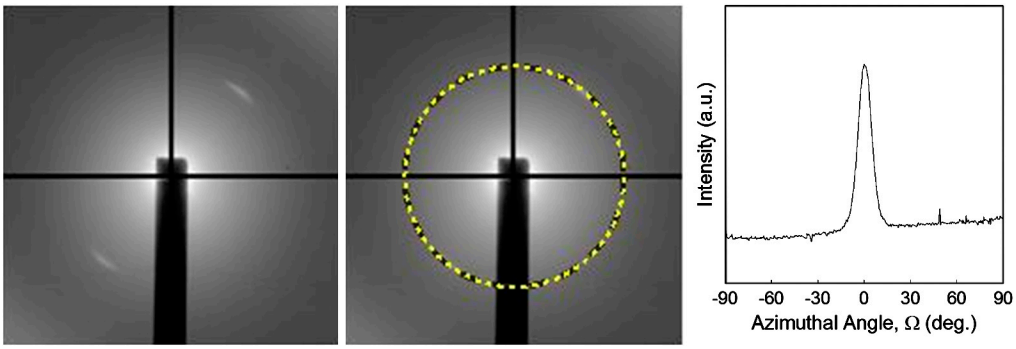

Fig. S9. Plot of the integrated intensities of the first order reflection as a function of azimuthal angle.